Lattice Strains at Cracks in Single Crystal Titanium: Elastic Distortion and GND Contributions

T. O. Erinosho* and F.P.E. Dunne
Department of Materials, Imperial College London, SW7 2AZ, London
***t.erinosho12@imperial.ac.uk**

Abstract

There is evidence from diffraction experiments that significant peak broadening is measured local to crack tips and this has been attributed to the development of geometrically necessary dislocations (GNDs) which are retained upon unloading. This is reasonable due to the stress singularity found locally at the crack which is expected to activate slip on favorably oriented slip systems, potentially resulting in plastic strain gradients and geometrically necessary dislocation development. Hence, a systematic study is presented here to ascertain the contributions of both elastic distortional strain and GND density to lattice deformation local to the crack at loaded and subsequently unloaded states.

The results show that whilst elastic strains dominate lattice distortion in comparison to GNDs at the loaded state i.e. at the peak load applied, these strains are largely recovered upon unloading and the contribution from GND development subsequently dominates the broadening seen. Two initial crystallographic configurations were considered. In the example in which the crystal c-axis was oriented parallel to the loading direction, the <c+a> pyramidal systems contributed most to slip with <a> basal slip system contributing to a lesser extent. However, in the example where the c-axis was oriented perpendicular to the loading direction, the <c+a> pyramidal and <a> prismatic systems were the more significant contributors to slip and the <a> basal contributing to a lesser extent. However, basal, prismatic and c+a pyramidal slip systems were found to be active in both examples and this was attributed to significant lattice rotation driven by locally high stresses which enabled otherwise badly oriented slip systems to become favourable for slip. Finally, increases in GND density were seen upon unloading for c-axis orientation parallel with loading. This was attributed to the influence of <c+a> pyramidal slip on reverse plasticity leading to diffuse GND density distributions and significant resulting lattice strains compared to that from <a> prism slip loading

Keywords: Crack tips, lattice strains, geometrically necessary dislocations, peak broadening, hcp crystals

1. Introduction

This paper aims to address elastic distortional strains and geometrically necessary dislocation (GND) content local to crack tips in single crystal titanium, and their role in lattice strain distributions and peak broadening. An x-ray with wavelength λ, incident on a single crystal is diffracted by plane normals in that crystal that satisfy Bragg's condition. The angle of diffraction, θ is obtained from Bragg's law such that

$$\boldsymbol{\lambda = 2d\sin\theta} \tag{1}$$

where d is the lattice spacing of the diffracting plane. The diffracted beam results in a point on a detector which translates to a delta function in intensity space representing the stress state of that plane. Assuming the plane is under zero stress, the delta peak remains in its ideal state. However, under an applied tensile or compressive stress, the lattice spacing d increases or decreases respectively and this further results in respective left and right shift of that peak. Consequently, a combination of crystallographic orientations that experience differing stress states (tensile and compressive) lead to shifts in the delta peak by differing amounts, thus, leading to a distribution. This distribution is referred to as a broadened peak which is indicative of the local stress states in the diffraction volume and has contributions from elastic strains and GND density which of course are also elastic in origin.

Previous work on FCC polycrystals by Erinosho et al. [1] has shown that both elastic deformation and GND density contribute to the broadened peak and that the contributions from GNDs potentially dominate measurements at large plastic strains. Furthermore, independent studies by Withers et al. [2] on peak width measurements (usually referred to as Full Width Half Maximum-(FWHM)) local to a crack tip show very high FWHMs which are hypothesized to significantly outweigh contributions from elastic deformation alone. Therefore, this work attempts to compute lattice distortion resulting from elastic strains and GNDs in view of relating this to experimental FWHM measurements.

Experimental evidence by Sun et al. [3] has shown that significant peak broadening local to a crack tip is caused by plasticity which is retained upon unloading. This further supports our hypothesis that diffraction peak broadening is found to be dominated by contributions from the development of geometrically necessary dislocation (GND)-controlled lattice curvature compared to stress-controlled elastic distortions. Whilst both drivers are elastic in origin, we differentiate between them and their respective contributions to lattice strain distributions. Prior to investigating deformation local to a crack tip due to the effects of elastic distortions and development of GND-controlled lattice curvature, the context and review of relevant literature is first presented.

The importance of structural integrity in materials in the presence of flaws (defects) has driven extensive investigations into crack tip deformation fields. Further, the associated biaxial stress state found local to the crack tip inhibits higher plastic strains to be developed in comparison to a uniaxial stress state. On this basis, Rice and coworkers [4, 5] developed an analytical asymptotic prediction of stresses ahead of a crack tip in elastic-ideally plastic face centered cubic (FCC) and body centered cubic (BCC) single crystals. This theory has been further developed by Gupta [6] to include the effects of material anisotropy by studying hexagonal closed packed (HCP) materials. Catoor and Kumar [7, 8] investigated crack-grain boundary interactions in zinc bicrystals both experimentally and computationally by considering crack growth on the basal plane in zinc using in-situ fracture testing of pre-cracked single crystals with emphasis on mechanisms that cause fracture. It was shown that the crystallographic orientation of crack growth direction on the basal plane influenced strain to failure and the nature of fracture. Subsequently, Olarnrithinun et al. [9] used discrete dislocation analysis to

study crack growth along the basal plane for two crack growth directions and showed that fracture toughness scales inversely with the tensile yield stress and is largely independent of plastic anisotropy. The issue of anisotropy effects at the crack tip was recently investigated by Kartal et al. [10] to evaluate the effects of crystallographic orientation and grain morphology on crack tip stress state and found that single crystal crack tip stresses largely remain independent of crystal orientation but that the plastic zone size and shape depends greatly upon it. Further studies include that by Biswas and Narasihman [11, 12] who investigated crack tip fields in rate sensitive FCC single crystals; Lopez-Crespo et al. [13, 14] who address overload effects during fatigue crack growth in steel using synchrotron x-ray diffraction for both plane strain and stress conditions, and studies by Kaushik et al. [15, 16] on experimental and finite element simulations of notch tip fields in magnesium single crystals.

However, of particular interest to the current study are the effects of cracks on diffraction peak broadening resulting from plastic strains developed local to the crack tip, and more particularly, the development of geometrically necessary dislocations (GNDs) which have been reported to be retained upon unloading [2, 3, 17, 18]. Diffraction experiments local to a crack carried out on steel have shown the development of large FWHM local to the crack tip [2]. Hence, this paper utilizes the methodology presented in [1] to address the contribution of elastic distortions and GND development to peak broadening at the loaded and unloaded states respectively. Also, an analysis of the slip systems contributing to plastic strains observed local to the crack tip is presented in the context of GND development and the activity of individual slip systems.

The crystal plasticity framework adopted is briefly described in §2 and the model used is presented in §3. §4 provides the methodology used to calculate the lattice distortion due to elastic strains and GNDs development in a defined process zone of an edge crack embedded in a 2-D plate. Finally, the results are presented in §5, discussion in section 6 and conclusions are presented in §7.

2. Crystal Plasticity Framework

The crystal plasticity framework adopted to investigate deformation in the process zone of a crack tip model is presented here. The framework used here was presented in previous studies by Erinosho et al. [19, 20] and is based on the kinematic decomposition of the deformation gradient $\boldsymbol{F}$ into elastic ($\boldsymbol{F}^{\mathrm{e}}$) and plastic ($\boldsymbol{F}^{\mathrm{p}}$) tensors as laid out by Lee [21] such that

$$\boldsymbol{F} = \boldsymbol{F}^{\mathrm{e}}\boldsymbol{F}^{\mathrm{p}}. \tag{2}$$

For simplicity, a power law relationship between slip rate and resolved shear stress for a given slip system is adopted and given by

$$\dot{\boldsymbol{\gamma}}^{\boldsymbol{\alpha}} = \dot{\boldsymbol{\gamma}}_{\mathbf{0}} \left|\frac{\boldsymbol{\tau}^{\boldsymbol{\alpha}}}{\mathbf{g}^{\boldsymbol{\alpha}}}\right|^{\boldsymbol{n}} \mathbf{sgn}(\dot{\boldsymbol{\gamma}}) \tag{3}$$

where the slip rate ($\dot{\gamma}^{\alpha}$) evolves on individual slip systems (α) and depends on the reference strain rate, $\dot{\gamma}_0^{\alpha}$, resolved shear stress, τ^{α}, and slip system strength, g^{α}. Note that there is some slip for all non-zero levels of shear stress in Eq. 3. However, the chosen value of exponent *n* ensures that below the critical value, the slip rate is effectively zero and only becomes significant once the critical level of stress is attained. Hardening is incorporated through the evolution of g^{α} in Eq. 3. Whilst a range of latent hardening forms can be adopted as outlined by Asaro [22]**,** isotropic hardening is employed here for simplicity such that all slip systems undergo the same level of hardening equal to that developed on the slip system with the maximum slip. Hence, the slip system strength evolution is given by

$$\dot{g}^{\alpha} = h_0\left(1 + \frac{h_0\gamma_{\text{sum}}}{q_0 m}\right)^{m-1}(\dot{\gamma})_{\max} \tag{4}$$

in which the accumulated slip is calculated from

$$\gamma_{\text{sum}} = \sum_{\beta=1}^{N_{\text{slip}}}\left(\int_0^t \dot{\gamma}^{\beta} dt\right). \tag{5}$$

The hardening properties used in the slip rule are summarized in Table 1 and the range of hcp slip systems incorporated in this formulation are shown in Fig. 1. The slip systems include the <a> basal, <a> prismatic, <a> pyramidal and the 1st and 2nd order <c+a> pyramidal systems and the slip strength of each system given by the critical resolved shear stress (CRSS) is specified in Table 2 obtained from Gong et al. [23].

The development of GND density local to the crack tip forms an integral part of the current study. Hence, GND density is calculated using a decoupled approach which uses the plastic strains at integration points to calculate the Burger's vector discontinuities which are translated to GND densities through use of the Nye tensor as follows

$$\sum_{\alpha=1}^{N} \boldsymbol{b}_{\text{G}}^{\alpha} \otimes \boldsymbol{\rho}_{\text{G}}^{\alpha} \equiv \text{Curl}(\boldsymbol{F}^{\text{p}}) \tag{6}$$

where the GND densities are summed over all slip systems (α) of edge and screw type and $\text{Curl}(\boldsymbol{F}^{\text{p}})$ is calculated in the undeformed state. The left-hand term may be decomposed in terms of dislocations of edge and screw type by $\sum_{\alpha=1}^{N} \boldsymbol{b}_{\text{G}}^{\alpha} \otimes \boldsymbol{\rho}_{\text{G}}^{\alpha} \equiv \sum_{\alpha=1}^{N}(\boldsymbol{b}_{\text{e}}^{\alpha} \otimes \boldsymbol{\rho}_{e}^{\alpha} + \boldsymbol{b}_{s}^{\alpha} \otimes \boldsymbol{\rho}_{\text{s}}^{\alpha})$ where $\boldsymbol{b}_e$ and $\boldsymbol{b}_s$ represent edge and screw type Burger's vectors and $\boldsymbol{\rho}_e$ and $\boldsymbol{\rho}_s$ are the edge and screw type GND densities respectively. Note that whilst both edge and screw components can in principle be considered, only the edge components are used in Eq. (6) in the present 2D analysis for the purposes of simplicity.

The LHS of Eq. 6 can be written more specifically for HCP such that

$$\begin{aligned}\boldsymbol{b}_{\text{G}}^{\alpha} \otimes \boldsymbol{\rho}_{\text{G}}^{\alpha} = &(\boldsymbol{b}_{\text{G}}^{\text{<a>basal}} \otimes \boldsymbol{\rho}_{\text{G}}^{\text{<a>basal}}) + (\boldsymbol{b}_{\text{G}}^{\text{<a>pris}} \otimes \boldsymbol{\rho}_{\text{G}}^{\text{<a>pris}}) + (\boldsymbol{b}_{\text{G}}^{\text{<a>pyra}} \otimes \boldsymbol{\rho}_{\text{G}}^{\text{<a>pyra}}) + \\ &(\boldsymbol{b}_{\text{G}}^{\text{<c+a>pyra}} \otimes \boldsymbol{\rho}_{\text{G}}^{\text{<c+a>pyra}})\end{aligned} \tag{7}$$

Eqs. (6) and (7) are under-defined and are solved using the L^1 method, which considers the dislocation as a line through a volume. The dislocation line energy is then minimized by finding the dislocation configuration with the smallest total line length [24]. Note that it is important to account for the energies on the individual slip system types in the HCP formulation in order to capture the relative ease of GND accumulation on <a> type slip systems compared to the <c+a> slip systems.

3. Crack tip model

Crack Tip Model

Fig. 2a shows the schematic of the 2-D model used to investigate deformation local to the crack tip. The plane stress model was built in ABAQUS with dimensions $100 \times 100\mu\text{m}^2$ and an edge crack of length $a = 20\mu\text{m}$ was incorporated at h=50μm. Whilst a 3-D plane strain model could be adopted, 2-D plane stress is considered for computational efficiency. Although this is a simplification of a 3-D problem, it is widely adopted in the mechanics community as a good approximation to tackle crack tip problems.

Further, a remote stress $\sigma_0 = 60\text{MPa}$ was applied in the Y-direction and a region *r* was defined along the length of the crack. The schematic in Fig. 2a was then meshed as shown in Fig. 2b. A coarse mesh was adopted remote from the crack but local to the crack, a fine mesh is utilised in order to adequately capture the effects of the crack singularity. The region local to the crack was then discretized into two regions referred to as Regions A and B shown in Fig. 2b local to the crack. Note that Region A is circular with a diameter of $0.2\mu\text{m}$ while Region B is a subset of Region A. This model will now be used to investigate lattice deformation local to a crack tip due to elastic strains and GND development.

4. Computing lattice distortion due to elastic strains and GNDs

The methodology presented in [1] is adopted to examine the crystal lattice spacing distortions due to elastic strains and GND development at the crack tip. The lattice spacings between corresponding crystal planes change with elastic strain, and the elastic deformation gradient $\boldsymbol{F}^{\text{e}}$ may be used to determine the resulting lattice spacings due to elastic distortions as follows

$$\frac{a'_{\text{e}}}{a_0} = |\boldsymbol{F}^{\text{e}}\boldsymbol{e}_1^{\text{c}}|, \frac{b'_{\text{e}}}{b_0} = |\boldsymbol{F}^{\text{e}}\boldsymbol{e}_2^{\text{c}}|, \frac{c'_{\text{e}}}{c_0} = |\boldsymbol{F}^{\text{e}}\boldsymbol{e}_3^{\text{c}}| \tag{8}$$

where $a_0 = b_0 = 2.95$ Angstroms and $c_0 = 4.68$ Angstroms are the undeformed lattice lengths and $\boldsymbol{e}_1^{\text{c}}$, $\boldsymbol{e}_2^{\text{c}}$ and $\boldsymbol{e}_3^{\text{c}}$ are unit orthogonal vectors rotated into the (deformed) crystallographic configuration. That is,

$$\boldsymbol{e}_i^{\text{c}} = \Delta\boldsymbol{R}^{\text{c}}\boldsymbol{R}_0^{\text{c}}\boldsymbol{e}_i \tag{9}$$

where *i* =1, 2 and 3 correspond to the x, y, and z directions respectively and $\boldsymbol{R}_0^{\text{c}}$ is a rotation matrix which maps the undeformed crystal to the local crystallographic configuration. $\Delta\boldsymbol{R}^{\text{c}}$ which is obtained from the polar decomposition of $\boldsymbol{F}$ maps the local crystal orientation into the deformed state. Full details of the crystal orientation mappings can be found in [1].

Next, the lattice distortion due to GND development is required. Consider the anticlockwise Burgers circuit enclosed by $\boldsymbol{d}_1$, $\boldsymbol{d}_2$, $\boldsymbol{d}_3$ and $\boldsymbol{d}_4$ shown in Fig. 3a. The net Burger's vector can be calculated using

$$\boldsymbol{d}_1 + \boldsymbol{d}_2 + \boldsymbol{d}_3 + \boldsymbol{d}_4 = 0 \Rightarrow \oint_{\Gamma} \boldsymbol{F}^{\text{P}}\, dX = 0 \tag{10}$$

where $\boldsymbol{F}^{\text{P}}$ is the plastic deformation gradient obtained in Eq. (2). A similar loop in a distorted plane shown in Fig. 3b shows an extra plane of atoms resulting in a net Burger's vector, $\boldsymbol{B}$. Using stokes law applied to our finite element framework, a length normalized Burger's vector $\boldsymbol{B}^l$ can be obtained around the path Γ on an infinitesimal surface, *S*, with normal $\boldsymbol{n}$, with knowledge of the local plastic deformation gradient ($\text{Curl}\boldsymbol{F}^{\text{p}}$) such that

$$\boldsymbol{B}^l \cong \text{Curl}(\boldsymbol{F}^{\text{P}})\boldsymbol{n}\frac{\Delta A}{L}. \tag{11}$$

ΔA is the surface area of each finite element and L is the associated length scale of the discretized region with normal $\boldsymbol{n}$. Note, $\boldsymbol{n}$ is the unit normal to the slip plane in the reference configuration. The region of interest (Region B) defined in Fig. 2b has a length of $0.08\mu\text{m}$ and was discretized into a 40×40 grid as illustrated in Fig. 4 in order to adequately capture the local variation of plastic strain. Thus, each discretized region which now has an associated length scale of $L \sim 0.003\mu\text{m}$ was assumed to have constant strain. Consider a particular discretized region indicated in Fig. 4. The plastic strain gradient is calculated by adopting a non-local approach by considering the variation of plastic strain in two neighboring regions in

the X- and Y-directions respectively. Note that $\boldsymbol{B}^l$ can be calculated on any arbitrary plane with normal $\boldsymbol{n}$ in the HCP crystal using the 3-index system as demonstrated in [1] such that the contribution of the normalized Burgers vector discontinuity $\boldsymbol{B}^l$ to lattice deformation can then be calculated. Whilst the 3-index system is unconventional for HCP crystals, it provides a commonality in methodology across all crystal types. Hence, we adopt a lattice distortion gradient, $\boldsymbol{F}^{\mathrm{gnd}}$, from [1] such that

$$\boldsymbol{F}^{\mathrm{gnd}} = \begin{pmatrix} 1+\boldsymbol{B}^l{}_1 \cdot \boldsymbol{e}'_1 & \boldsymbol{B}^l{}_2 \cdot \boldsymbol{e}'_1 & \boldsymbol{B}^l{}_3 \cdot \boldsymbol{e}'_1 \\ \boldsymbol{B}^l{}_1 \cdot \boldsymbol{e}'_2 & 1+\boldsymbol{B}^l{}_2 \cdot \boldsymbol{e}'_2 & \boldsymbol{B}^l{}_3 \cdot \boldsymbol{e}'_2 \\ \boldsymbol{B}^l{}_1 \cdot \boldsymbol{e}'_3 & \boldsymbol{B}^l{}_2 \cdot \boldsymbol{e}'_3 & 1+\boldsymbol{B}^l{}_3 \cdot \boldsymbol{e}'_3 \end{pmatrix}. \tag{12}$$

Here, $\boldsymbol{B}^l{}_1$, $\boldsymbol{B}^l{}_2$ and $\boldsymbol{B}^l{}_3$ represent the discontinuities on the (100), (010) and (001) planes respectively and $\boldsymbol{e}'_1$, $\boldsymbol{e}'_2$, and $\boldsymbol{e}'_3$ are unit vectors [100], [010] and [001] rotated into the local crystallographic configuration. That is, $\boldsymbol{e}'_i = \boldsymbol{R}^c_0 \boldsymbol{e}_i$ where i =1,2 3 and $\boldsymbol{R}^c_0$ is a rotation matrix which maps the underformed crystal to its local crystallographic orientation. $\boldsymbol{F}^{\mathrm{gnd}}$ is then calculated in the deformed crystallographic configuration using

$$\boldsymbol{F}^{\mathrm{gnd}\prime} = \Delta\boldsymbol{R}^{\mathrm{c}}\boldsymbol{F}^{\mathrm{gnd}} \tag{13}$$

where $\Delta\boldsymbol{R}^{\mathrm{c}}$ represents lattice rotations from the local crystallographic configuration to the deformed state and, the lattice distortion due to GNDs is calculated using Eq. 8 by replacing $\boldsymbol{F}^{\mathrm{e}}$ with $\boldsymbol{F}^{\mathrm{gnd}\prime}$.

Finally, the lattice spacing for all possible *hkl* planes in an HCP crystal can be obtained using [25]

$$d_{hkl} = \frac{\sqrt{3}}{2}\sqrt{\frac{a^2}{h^2+hk+k^2} + \frac{c^2}{l^2}}. \tag{14}$$

5. Results

5.1. Elastic response in process zone

The lattice response to elastic strain local to the crack tip is investigated first. Although it is expected that stress singularity local to the crack tip should typically activate slip on favourably oriented slip systems, only the elastic strains developed due to the applied remote stress are obtained. The methodology in the previous section is applied to Region B shown in Fig. 2 to calculate the lattice spacings due to elastic distortions for the basal plane of each element shown. Note that all distances in Region B are measured from the reference point indicated in Fig. 2b and are normalized using the length of the region (0.08μm).

Fig. 5 shows the lattice distortion due to elastic strains for differing crystallographic configurations at the loaded state (point B) illustrated in Fig. 5ai. The crystallographic configurations considered are shown in Figs. 5aii and 5aiii. Note that in Fig. 5aii, the c-axis in the HCP crystal is parallel to the loading direction but, in Fig. 5aiii, the c-axis is perpendicular to the loading direction. Fig. 5bi shows a schematic of the basal plane for which the lattice spacing due to elastic strains is calculated and shown in Figs. 5bii and 5biii.

Fig. 5bii shows the lattice spacings due to elastic strains on the basal plane for the initial crystallographic configuration shown in 5aii. In this configuration, the c-axis is parallel to the loading direction hence, an increase in the basal lattice spacing is expected. It is clear from Fig.

5bii that an increase is observed by noting the indicated ideal lattice spacing. The multi-axial stress state (i.e. biaxial state) local to the crack tip gives rise to the compressive stress state seen along the crack path. Now, consider Fig. 5biii which shows the lattice spacings of the basal plane for the crystallographic configuration shown in Fig. 5aiii for which the c-axis is perpendicular to the loading direction. A reduction in the spacing between consecutive basal planes is expected, at least remote from the crack tip. However, similar to the previous example, a multi-axial stress state local to the crack tip results in the tensile stresses seen along the crack path. Since elastic strains upon unloading shown later are recovered, this paper now focuses on the effects of plasticity in the process zone.

5.2. Plasticity in the process zone

The CRSS on each slip system specified in Table 2 was adopted to determine the onset of plasticity. The resulting plastic strains developed local to the crack tip within Region B of the crack model are shown in Fig. 6 for the two crystallographic configurations considered at the loaded and unloaded states respectively. Figs. 6ai and 6aii show the accumulated slip for the example in which the c-axis is parallel to the loading direction in the loaded and unloaded states respectively. Similarly, the accumulated slip is shown for the example with the c-axis perpendicular to the loading direction at the loaded and unloaded state shown in Figs. 6bi and 6bii respectively. It is clear from the accumulated slip fields shown that significant plastic strains develop local to the crack tip both at the loaded and unloaded states.

Now consider Fig. 7 which shows the GND density in process zone (Region B). Two initial crystallographic configurations are considered and for each example, the GND density at the loaded and unloaded states is shown. It is clear in both examples that GNDs developed at the crack tip during loading (Figs. 7ai and 7bi) and remain upon unloading (Figs. 7aii and 7bii). Although the GND fields are different depending on the initial crystallographic configuration, it is evident in both cases that the presence of the crack leads to concentrations of GND development.

Next consider Fig. 5 and 8 which compare the lattice distortion at the loaded state for the two initial crystallographic orientations considered, for which the elastic and GND distortion contributions are calculated using the methodology summarized in section 4. It may be seen that elastic distortional strains shown in Fig. 5 dominates at the loaded state, well over and above the contribution from GND development. However, Fig. 9 shows the lattice distortion distribution due to elastic strains and GND development upon unloading. In this instance, the elastic strains are mostly recovered at the unloaded state resulting in very limited contributions to lattice distortions due to elastic strains for both crystallographic configurations. However, at this state, the residual plastic strains result in GND development and the lattice contributions from GND density distributions become very significant.

A systematic evaluation of slip developed on each slip system type is analysed for varying crystallographic configurations in order to show how deformation is accommodated local to the crack tip and also, to understand which slip systems contribute to the GND densities developed. Fig. 10 shows the accumulated slip on individual slip systems for the two crystallographic configurations considered. Consider first the example in which the c-axis is parallel to the loading direction. It is expected that only <c+a> pyramidal planes are favorably oriented for slip. However, it is clear that the basal systems also contribute significantly and that the prismatic and <a> pyramidal systems are also activated local to the crack tip. Similarly, in the example where the c-axis is oriented perpendicularly to the loading direction, the

prismatic and <c+a> systems are oriented favorably for slip. However, the basal systems and <a> pyramidal systems are also found to be activated local to the crack tip.

Examination of the lattice rotations occurring for the crystallographic configurations considered shown in Fig. 11. Lattice rotation is measured in degrees and represents the rotation of the c-axis about the Z-direction. Note that positive and negative rotations are not distinguished. It is clear from Fig. 11 that significant lattice rotation is seen local to the crack tip thereby enabling otherwise badly oriented slip systems to become activated for slip. Hence, considering Fig. 10b in which the c-axis is parallel to the loading direction, it is clear from the rotation apparent in Fig. 11a that although only <c+a> systems are initially favoured for slip, basal systems also become activated. Further, the rotation also allows the activation of prismatic and <a> pyramidal slip albeit to a lower extent. This also applies to Fig. 10c such that rotations local to the crack tip allow the activation of otherwise inaccessible slip systems.

6. Discussion

Lattice distortions at crack tips due to elastic strains and GND density development respectively are evaluated in this paper. Although these individual contributions cannot be distinguished experimentally, the methodology presented by [1] provides the ability to differentiate the contributions from each mechanism. The development of plastic strain gradients and hence GND densities local to the crack tip are expected to translate to high GND densities which contribute to experimental diffraction peak broadening [2, 3, 17, 18].

Previous work by Erinosho et al. [1] demonstrates the methodology for differentiating between the contribution of elastic strains and GND development which of course, are also elastic in origin, to the overall lattice distortion. The methodology was applied here to consider a titanium single crystal with multi-axial (biaxial) stress state local to a crack tip. The motivation for this study was based on background experimental work that estimates the lattice strain Full Width Half Maximum (FWHM) local to a crack tip in polycrystal steel [2]. That study showed large FWHM local to the crack tip which was hypothesized to result from contributions other than elastic distortions alone.

An interesting outcome of the current work is the increase in GND density seen upon unloading for a specific orientation seen in Fig. 7. This is explained by examining the slip fields associated with each crystallographic orientation considered. Consider first the orientation in which the c-axis is perpendicular to the loading direction. Prismatic systems are favourably oriented for slip and rigid body rotation further leads to slip on the basal systems and limited slip activity on the pyramidal systems. Because of the relative ease of activating prism slip, the plastic straining is highly localised, reflecting a similarly localised distribution of lattice straining (Fig 8b). Whilst the GND density marginally increases in this orientation during unloading due to reversed slip, as do the lattice spacings, the influence of reverse plasticity is small. In the other orientation which has its c-axis parallel to the loading direction, the first factor is that c+a slip is hard to activate; a much higher resolved shear stress is needed, and the orientation largely precludes slip on other systems. Because of the crystal orientation and the intensification of stress at the crack tip, c+a slip is developed on loading generating a rather more diffuse but heterogeneous field of slip leading to a more diffuse distribution of GND density (Fig. 7ai) and hence lattice spacing change (Fig. 8a). On load reversal, given the high stresses achieved (giving rise to high elastic strains), a significant Bauschinger effect is anticipated with revered slip which similarly only activates at large reversed stress. A quite substantial increase in GND density results on load reversal which remains much more diffuse than that for prism slip. These conditions give rise to the resulting diffuse distribution of lattice strain changes which

are more significant than those for the prism slip loading. However, the absolute magnitude of GND density for the prism slip loading is rather similar to that for the c+a loading; the significant difference results from the more diffuse distribution of high GND density which occurs for the c-axis loading. This is further evident from the plastic strain fields seen in Figs. 10bv and 10cv. Similar differences between the loaded and unloaded states attributed to crack closure effects were also observed by Sun et al. [3] in steel.

The role of twinning has so far been neglected in the current study. Deformation by twinning is important to help accommodate lattice deformation in poorly oriented crystals for slip. For example, twin nucleation is likely to be activated in circumstances where the crystal c-axis is parallel to the loading direction. The manifestation of twinning is a large local lattice rotation to enable the activation of twin planes in order to accommodate slip. Whilst studies on magnesium by Kaushik et al. [15, 16] show the importance of twinning on deformation local to a crack tip, it is however ignored in this study.

7. Conclusions

An investigation into crack tip deformation is presented for single crystal titanium using crystal plasticity. A remote stress was applied to a 2-D single crystal plane stress model which was finely meshed local to the crack tip. A region of interest was selected local to the crack tip and an investigation into the elastic strains and development of GND density was carried out.

Evidence from diffraction experiments local to a crack tip show significant peak broadening typified by an increase in lattice distortion after unloading. This is reasonable due to stress singularity local to the crack tip which is expected to activate slip on favorably oriented slip systems. Thus, a systematic study was carried out to ascertain the contribution of elastic distortional strains and GND density to lattice deformation local to the crack tip at the loaded and unloaded states. The lattice distortion due to elastic strains was calculated from the elastic deformation tensor whilst the contribution of GNDs to lattice deformation was obtained by evaluating the contribution of the open Burger's vector to deformation.

The results show that whilst elastic strains dominate lattice distortion in comparison to GNDs at the loaded state i.e. at the peak load applied, these strains are mostly recovered upon unloading and the contribution from GNDs developed subsequently dominate the peak broadening seen. Two initial crystallographic configurations were considered. In the example in which the c-axis was oriented parallel to the loading direction, <c+a> pyramidal contributed mainly to slip and <a> basal slip to a lesser extent. However, in the example where the c-axis was oriented perpendicular to the loading direction, the <c+a> pyramidal and <a> prismatic systems were the more significant contributors to slip and the <a> basal to a lesser extent. However, all slip systems were active in both cases and this was attributed to lattice rotations driven by locally high stress and slip which enabled otherwise badly oriented slip systems to become favorable for slip.

It was also found that for the case of an edge crack within a single crystal with c-axis orientation parallel with the loading direction, unloading (following loading) was found to lead to considerable increases in local GND density, resulting in a consequent marked increase in lattice strains, whereas rather limited change under unloading was observed for the case in which the crystal c-axis was normal to the loading. Such marked differences may manifest themselves in diffraction experiments.

References

1. Erinosho, T.O. and F.P.E. Dunne, *Lattice strain distributions due to elastic distortions and GND development in polycrystals.* Journal of the Mechanics and Physics of Solids, 2014. **67**: p. 62-86.
2. Withers, P.J., *Fracture mechanics by three-dimensional crack-tip synchrotron X-ray microscopy.* Philosophical Transactions of the Royal Society a-Mathematical Physical and Engineering Sciences, 2015. **373**(2036).
3. Sun, Y., et al., *Changes in lattice-strain profiles around a fatigue crack through the retardation period after overloading.* Physica B-Condensed Matter, 2006. **385**: p. 633-635.
4. Rice, J.R., *Tensile Crack Tip Fields in Elastic Ideally Plastic Crystals.* Mechanics of Materials, 1987. **6**(4): p. 317-335.
5. Rice, J.R. and M. Saeedvafa, *Crack Tip Singular Fields in Ductile Crystals with Taylor Power-Law Hardening .1. Anti-Plane Shear.* Journal of the Mechanics and Physics of Solids, 1988. **36**(2): p. 189-214.
6. V, G., *Tensile Crack-Tip Fields in Elastic-Ideally Plastic Hexagonal Crystals and Layered Materials.* Acta Metallurgica Et Materialia, 1993. **41**(11): p. 3223-3236.
7. Catoor, D. and K.S. Kumar, *Crack growth on the basal plane in single crystal zinc: experiments and computations.* Philosophical Magazine, 2008. **88**(10): p. 1437-1460.
8. Catoor, D. and K.S. Kumar, *Crack-grain boundary interactions in zinc bicrystals.* Philosophical Magazine, 2011. **91**(16): p. 2154-2185.
9. Olarnrithinun, S., S.S. Chakravarthy, and W.A. Curtin, *Discrete dislocation modeling of fracture in plastically anisotropic metals.* Journal of the Mechanics and Physics of Solids, 2013. **61**(6): p. 1391-1406.
10. Kartal, M.E., M.A. Cuddihy, and F.P.E. Dunne, *Effects of crystallographic orientation and grain morphology on crack tip stress state and plasticity.* International Journal of Fatigue, 2014. **61**(0): p. 46-58.
11. Biswas, P. and R. Narasimhan, *Quasi-static crack tip fields in rate-sensitive FCC single crystals.* Sadhana-Academy Proceedings in Engineering Sciences, 2012. **37**(1): p. 149-169.
12. Narasimhan, R., et al., *Stationary crack tip fields in elastic-plastic solids: an overview of recent numerical simulations.* Journal of Physics D-Applied Physics, 2009. **42**(21).
13. Lopez-Crespo, P., et al., *Overload effects on fatigue crack-tip fields under plane stress conditions: surface and bulk analysis.* Fatigue & Fracture of Engineering Materials & Structures, 2013. **36**(1): p. 75-84.
14. Lopez-Crespo, P., et al., *Measuring overload effects during fatigue crack growth in bainitic steel by synchrotron X-ray diffraction.* International Journal of Fatigue, (0).
15. Kaushik, V., R. Narasimhan, and R.K. Mishra, *Finite element simulations of notch tip fields in magnesium single crystals.* International Journal of Fracture, 2014. **189**(2): p. 195-216.
16. Kaushik, V., R. Narasimhan, and R.K. Mishra, *Experimental study of fracture behavior of magnesium single crystals.* Materials Science and Engineering a-Structural Materials Properties Microstructure and Processing, 2014. **590**: p. 174-185.
17. Smith, J., et al., *Measurement of Crack-Tip Strains Using Neutron-Diffraction.* Engineering Fracture Mechanics, 1995. **52**(5): p. 843-851.
18. Lee, S.Y., et al., *Neutron and X-ray Microbeam Diffraction Studies around a Fatigue-Crack Tip after Overload.* Metallurgical and Materials Transactions a-Physical Metallurgy and Materials Science, 2008. **39A**(13): p. 3164-3169.
19. Erinosho, T.O., A.C.F. Cocks, and F.P.E. Dunne, *Coupled effects of texture, hardening and non-proportionality of strain on ductility in ferritic steel.* Computational Materials Science, 2013. **80**: p. 113-122.
20. Erinosho, T.O., A.C.F. Cocks, and F.P.E. Dunne, *Texture, hardening and non-proportionality of strain in BCC polycrystal deformation.* International Journal of Plasticity, 2013. **50**: p. 170-192.
21. Lee, E.H., *Elastic-Plastic Deformation at Finite Strains.* Journal of Applied Mechanics, 1969. **36**(1): p. 1-&.
22. Asaro, R.J., *Micromechanics of Crystals and Polycrystals.* Advances in Applied Mechanics, 1983. **23**: p. 1-115.
23. Gong, J.C. and A.J. Wilkinson, *Anisotropy in the plastic flow properties of single-crystal alpha titanium determined from micro-cantilever beams.* Acta Materialia, 2009. **57**(19): p. 5693-5705.
24. Arsenlis, A. and D.M. Parks, *Crystallographic aspects of geometrically-necessary and statistically-stored dislocation density.* Acta Materialia, 1999. **47**(5): p. 1597-1611.
25. Cullity, B.D. and S.R. Stock, *Elements of X-ray diffraction*. 3rd ed. 2001, Upper Saddle River: Prentice Hall. xviii, 664 p.

Table 1

Material properties of Titanium used in the slip rule calibrated using single crystal Titanium mechanical response in Gong et al. [23]

h_0	n	$\dot{\gamma}_0$	m	q_0
0.0025GPa	50	$1s^{-1}$	0.245	70MPa

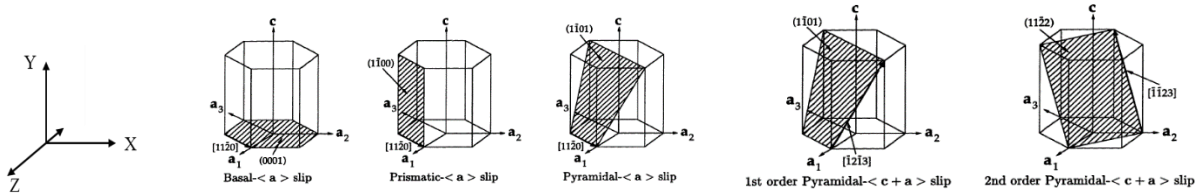

Fig. 1. The range of HCP slip systems incorporated into the crystal plasticity calculations each having CRSS values specified in Table 2.

Table 2

Slip system properties of Titanium obtained from Gong et al. [23]

	Basal	**Prismatic**	**<a>Pyramidal**	**<c+a>Pyramidal**
CRSS (MPa)	208	180	474	474

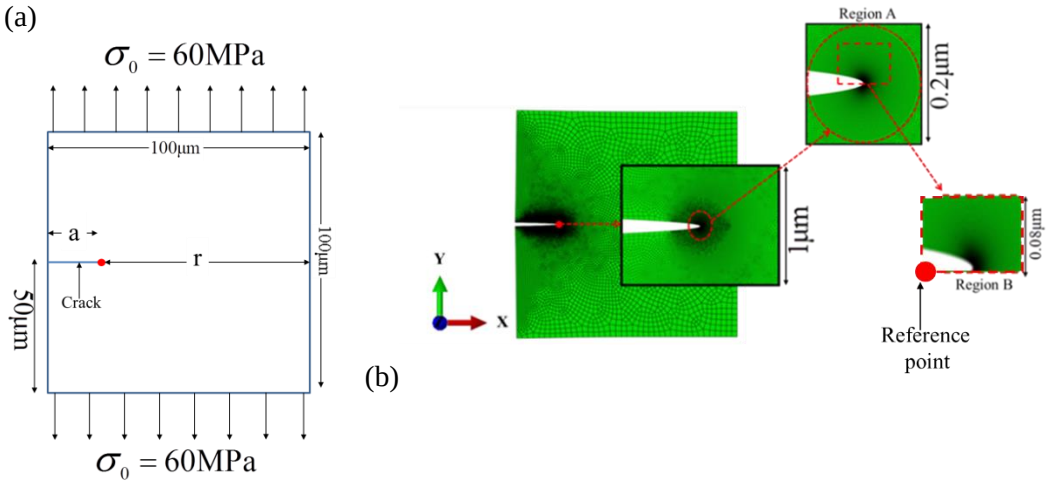

Fig. 2. (a) Schematic of $100 \times 100\mu m^2$ 2-D single crystal plate with an embedded edge crack of length $a = 20\mu m$. The plate is meshed as shown in (b) and two regions of interest are defined. Region A is circular with diameter $0.2\mu m$ and Region B is a subset of A and has dimensions $0.08 \times 0.08\mu m^2$.

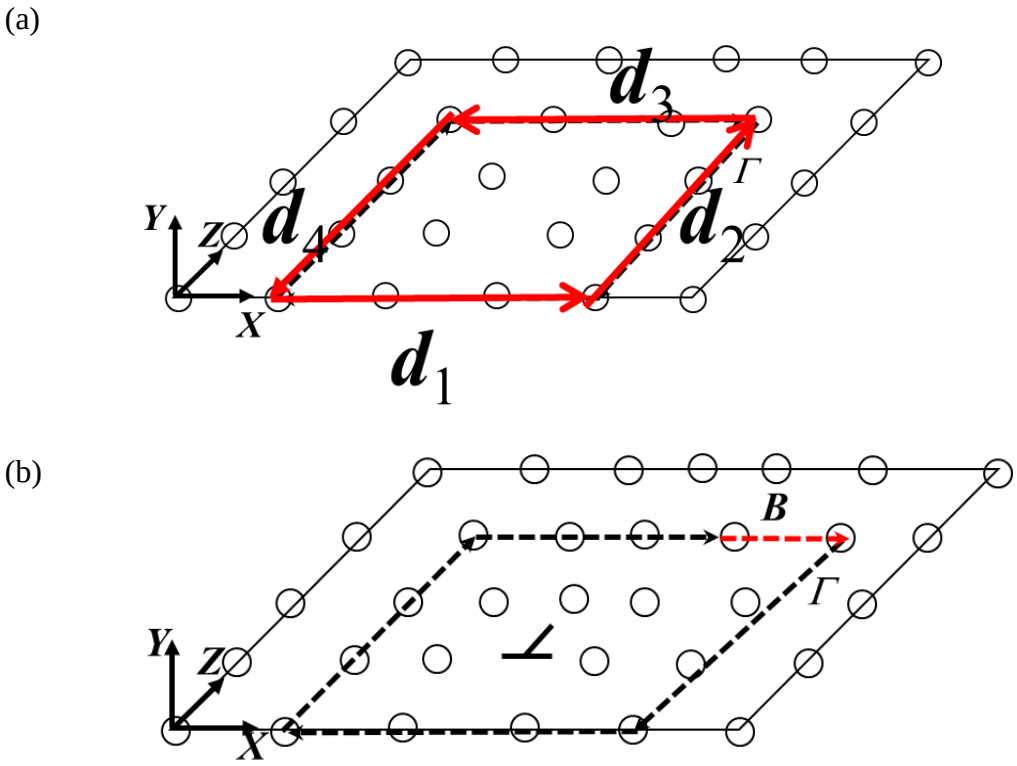

Fig. 3: Schematic diagram showing a plane of atoms indicating (a) a closed Burger circuit with zero resultant dislocation, (b) an open Burger's circuit with a residual dislocation of geometric consequence shown by the vector ***B***.

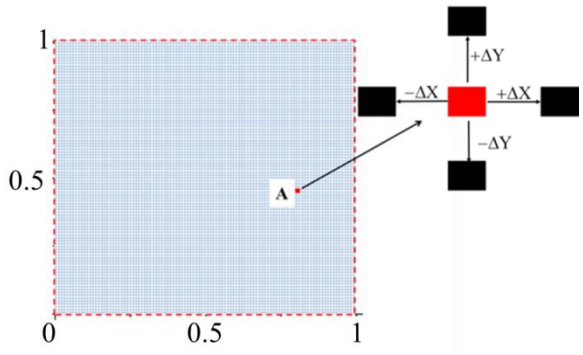

Fig. 4. Schematic of the discretization process used to calculate GND density. The plastic deformation gradient (curl $\boldsymbol{F}^{p}$) is calculated in each discretized region using the detailed non-local approach similar to that adopted by [1].

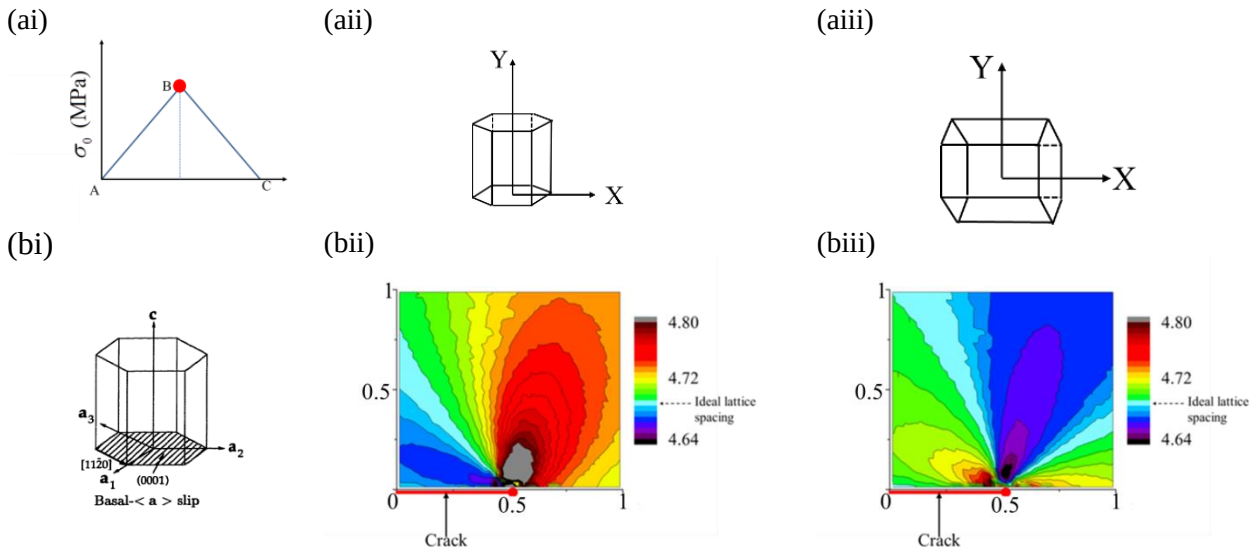

Fig. 5. Basal lattice spacings in Angstroms due to elastic strains for the crack tip model shown in Fig. 2. The loading condition is shown in (ai), and the initial crystallographic configurations are shown in (aii) and (aiii). An example showing a typical basal plane is shown in (bi) and the lattice distortions due to elastic straining are shown for the corresponding crystallographic configurations in (bii) and (biii).

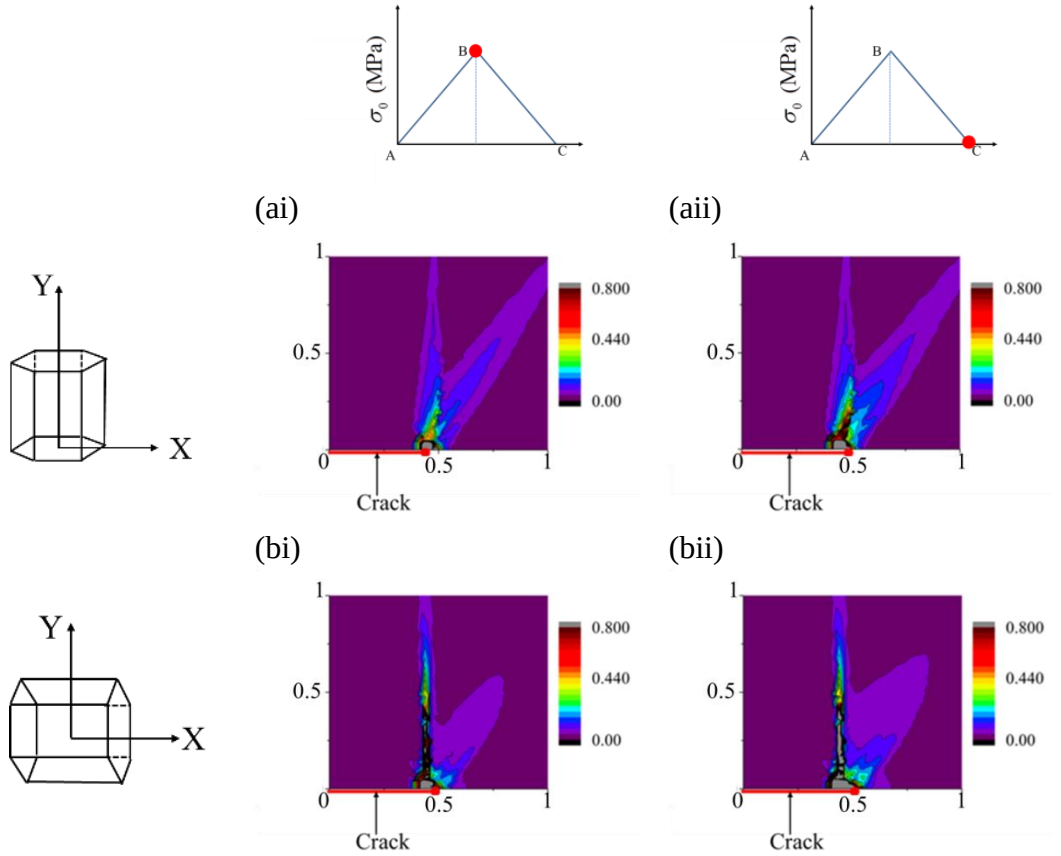

Fig. 6. Contour distribution of accumulated plastic strain for the two initial crystallographic configurations considered at the loaded and unloaded states.

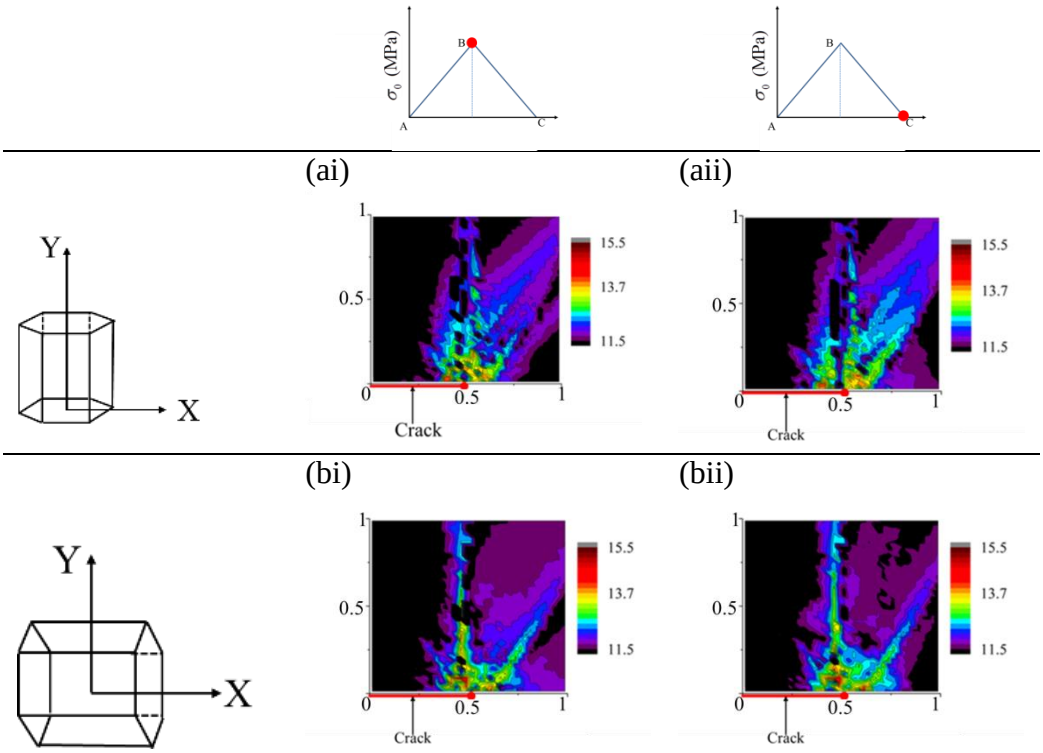

Fig. 7. Contour distribution of GND density in Region B illustrated in Fig. 2b. The densities are measured in $Log_{10}(m^{-2})$ and are shown for each crystallographic configuration at the loaded and unloaded states. Note, the L^1 minimization method is used and only the edge components of dislocations are used in Eq. (6) to obtain GND densities.

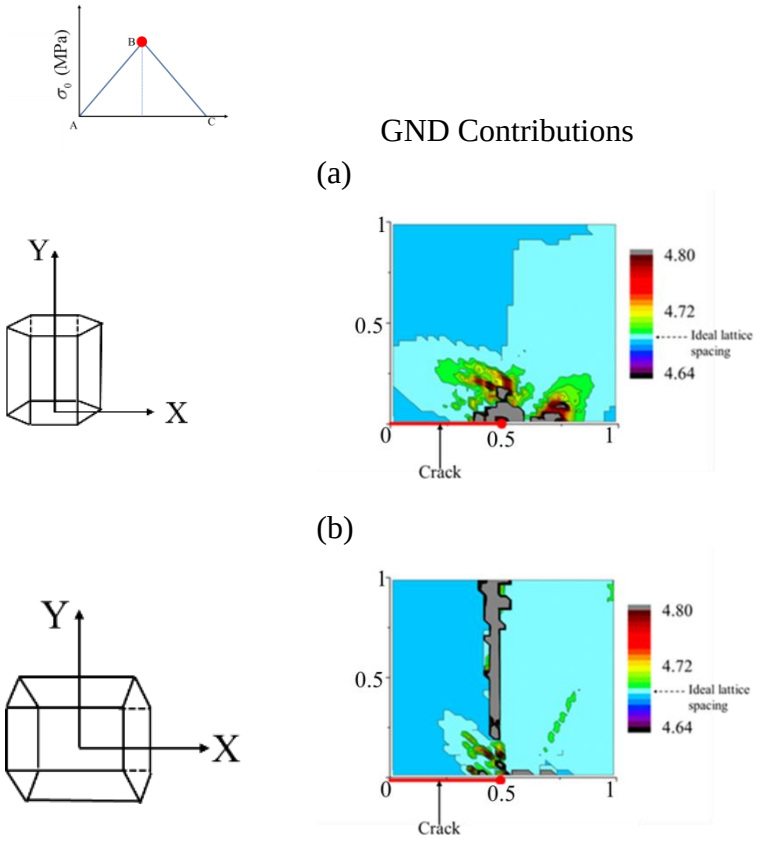

Fig. 8. Basal lattice spacings (Angstroms) due to elastic strains and GND development at the loaded state for the two initial crystallographic orientations shown. Refer to Fig. 5 for the basal lattice contributions from elastic distortions.

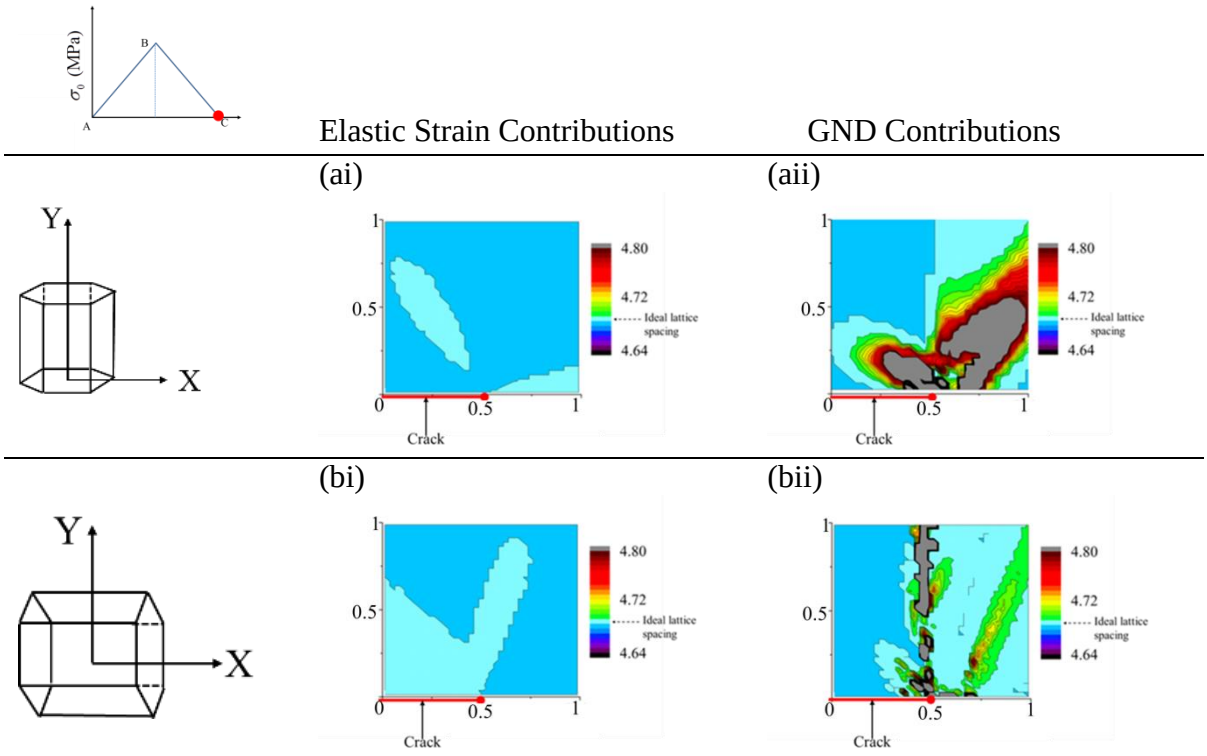

Fig. 9. Basal lattice spacings (Angstroms) for basal plane due to elastic strains and GND development at the unloaded state for the two crystallographic orientations shown.

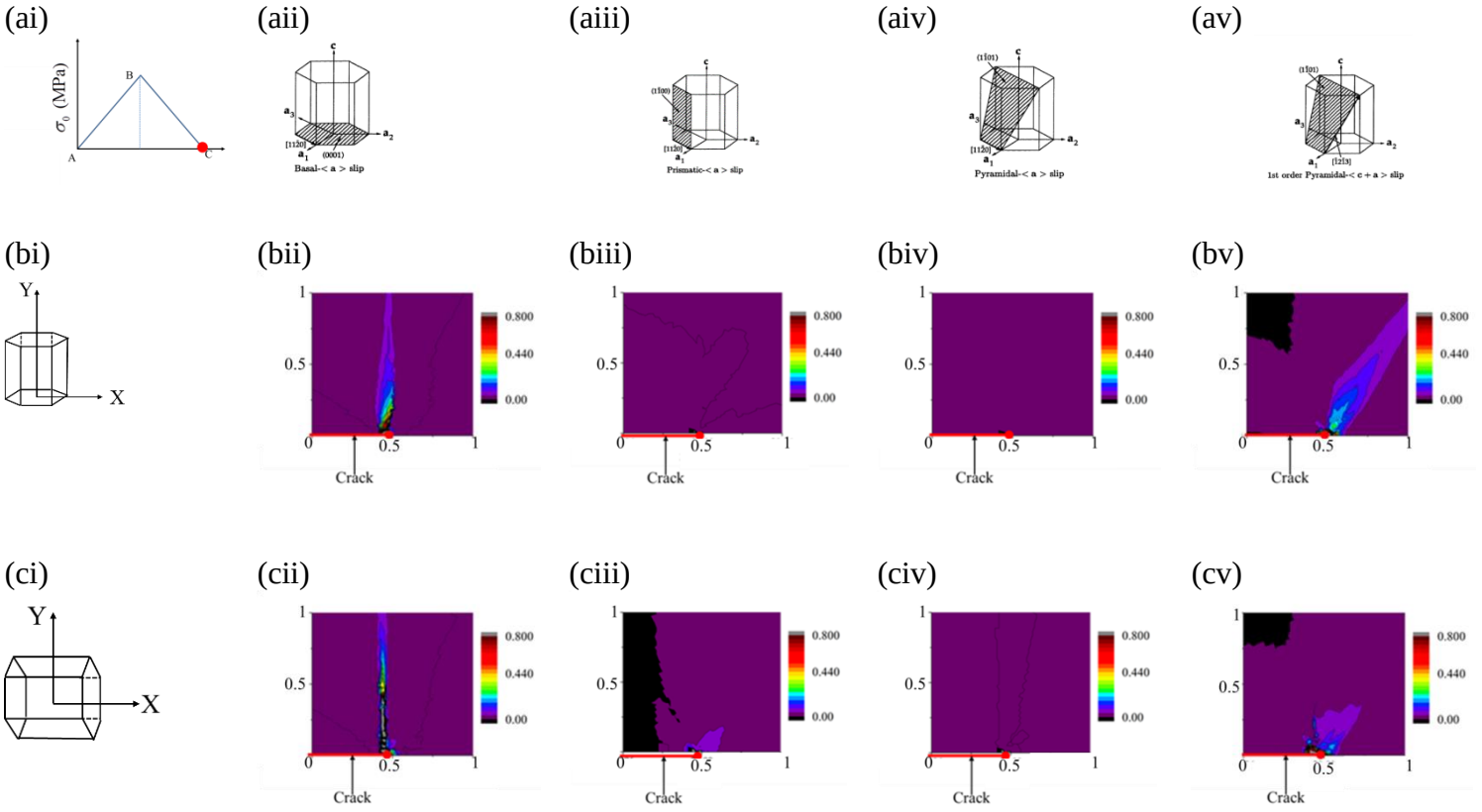

Fig. 10. Contour distribution of accumulated slip on individual slip systems for the crystallographic orientations shown at the unloaded state. For both configurations, basal plane slip is shown in (bii) and (cii), prismatic plane slip in (biii) and (ciii), <a> pyramidal plane slip in (biv) and (civ) and finally, the <c+a> pyramidal slip in (bv) and (cv).

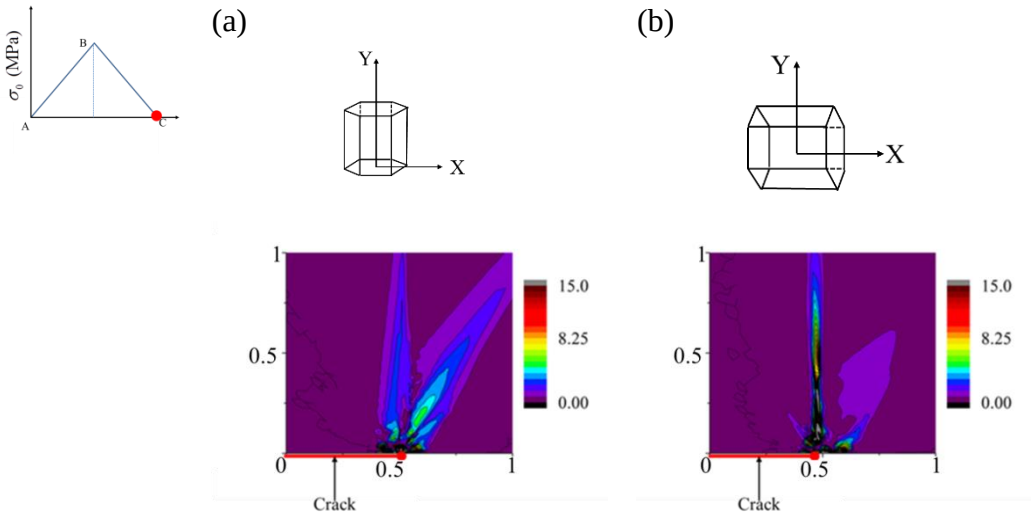

Fig. 11. Contour distribution of lattice rotation ($\Delta \boldsymbol{R}^{c}$) measured in degrees for the crystallographic orientations shown.